Applied Energy 231 (2018) 399–411

Contents lists available at ScienceDirect

Applied Energy

journal homepage: www.elsevier.com/locate/apenergy

Energy management for a grid-connected wave energy park through a hybrid energy storage system

Arvind Parwal[a,*], Martin Fregelius[a], Irinia Temiz[a], Malin Göteman[a], Janaina G. de Oliveira[a,c], Cecilia Boström[a], Mats Leijon[a,b]

[a] Division of Electricity, Department of Engineering Sciences, Swedish Centre for Renewable Electric Energy Conversion, Uppsala University, Box 534, SE-751 21 Uppsala, Sweden
[b] Department of Electrical Engineering, Chalmers University of Technology, 412 96 Gothenburg, Sweden
[c] Universidade Federal de Juiz de Fora, Brazil

HIGHLIGHTS

- Introducing an energy management system with a dynamic rate limiter control.
- Exemplified by using a wave energy-park as an input power source.
- Battery and controller losses are reduced with improved state-of-charge control.
- Analysis and verification of adequate control for power-sharing over the hybrid energy storage.
- A steady and improved power quality is ensured.

GRAPHICAL ABSTRACT

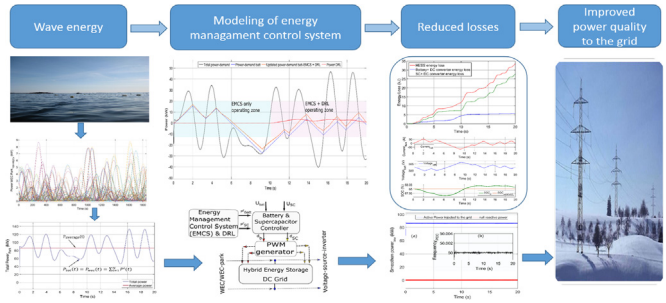

ARTICLE INFO

Keywords:
Wave energy converter
Hybrid energy storage system
Energy management control system
Dynamic rate limiter
State of charge

ABSTRACT

The concern for climate change and energy consumption has increased the demand for renewable energy production considerably. Marine energy sources attract attention because of their high energy density. Wave energy is an attractive renewable energy source with large potential. Due to the nature of the ocean waves, a linear wave energy converter generates intermittent power. It is therefore crucial to regularize the power before connecting to the grid. Energy storage systems present effective ways to minimize the power fluctuations and deliver a steady power to the grid. In this paper, we present an energy management control system with a dynamic rate limiter. The method is applied to control a hybrid energy storage system, combining battery and supercapacitor, with a fully active topology controlled by the power converters. The results show that the method is able to control the charging and discharging states of the battery and the supercapacitor, and minimize the power fluctuation to the grid. The algorithm ensures low losses by shifting the required power and the stored power smoothly over the energy storage system.

1. Introduction

Sustainable energy sources are increasingly recognized as a cost-effective renewable energy sources to satisfy the growing energy demand [1]. Using renewable sources can reduce the system cost considerably and could make a significant contribution to the demand in energy [2]. Appino et al. studied a hierarchical scheduling and control scheme for a grid connected system [3], where a dispatch schedule is

* Corresponding author.
E-mail address: arvind.parwal@angstrom.uu.se (A. Parwal).

https://doi.org/10.1016/j.apenergy.2018.09.146
Received 20 April 2018; Received in revised form 20 August 2018; Accepted 13 September 2018
Available online 20 September 2018
0306-2619/ © 2018 Elsevier Ltd. All rights reserved.

Nomenclature

Abbreviations

BW	bandwidth
C	capacitance (F)
d_{batt}	allowed power fluctuation for the battery for the considered time period T
d	duty ratio for the supercapacitor controller
d_b	duty ratio for the battery controller
DRL	dynamic rate limiter
E_{HESS}	energy in the HESS (Wh)
EMCS	energy management control system
ESS	energy storage system
f_c	crossover frequency (kHz)
f_{cb}	crossover frequency of the battery (kHz)
f_{sw}	switching frequency (kHz)
HESS	hybrid energy storage system
I_{DC}	DC-grid current (A)
i_{ref_dem}	referenced demand current (A)
i_{ref_batt}	referenced current for the battery (A)
i_{ref_t}	total reference current (A)
I_{sc},I_L	supercapacitor inductor current (A)
$K_{p,sc}$	proportional gain for the PI-controller of SC
$K_{p,b}$	proportional gain for the PI-controller of the battery
$K_{i,b}$	integral gain for the PI-controller of the battery
$K_{i,sc}$	integral gain for the PI-controller of SC
L	SC connected DC/DC converter inductance (mH)
L_b	battery connected DC/DC converter inductance (mH)
Li-ion	lithium-ion
LPF	low pass filter
$P_{average}(t)$	average power component (kW)
$P_{Batt}(t)$	battery power (kW)
$P^r_{Batt}(\Delta t)$	updated power demand for the battery (kW)
$P_{grid}(t)$	grid power (kW)
$P_{HESS}(t)$	HESS power (kW)
$P_{HESS,max}$	maximum power of the HESS (kW)
$P^{new}_{HESS}(t)$	new power demand for the HESS (kW)
$P_{\overline{HESS}}(t)$	filtered variable of power component (kW)
$P_{inv}(t)$	inverter output power (kW)
$P^r_{SC}(\Delta t)$	updated power demand for the SC
$P_{WEC}(t)$	wave energy park power output (kW)
PCC	point of common coupling
PI	proportional and integral
PM	phase margin (°)
PWM	pulse width modulator
$r_{batt}(t)$	rate of power change for the battery
R_{lp}	inductor parasitic resistance (mΩ)
R_{on}	turn-on resistance (mΩ)
r_p	parasitic resistance (mΩ)
r_{ib}	battery internal resistance (mΩ)
R	resistance (Ω)
SC	supercapacitor
SISO	single input single output
SOC	state-of-charge
SOC_m	measured value of the SOC (%)
SOC^{max}	maximum value of the SOC of the battery
SOC^{min}	minimum value of the SOC of the battery
SOC_{ref}	referenced value of the battery SOC (%)
SOC^{SC}_{ref}	referenced value of the SC SOC (%)
T	considered time period for the battery fluctuations (s)
t	time (s)
T_w	observed time interval (s)
v_{Batt}	voltage of the battery (V)
V_{DC}	DC-link voltage (V)
V_{ref}	referenced DC-link voltage (V)
VSI	voltage source inverter
WEC	wave energy converter
WEP	wave energy park
Δt	change in each time iteration (s)
ΔP_{Batt}	DRL power output (kW)
α^{rise}_{batt}	rising rate limiter
α^{fall}_{batt}	falling rate limiter
δ_i	SOC based function for the DRL
ρ_i	the variable accelerator
τ	time constant for the low pass filters

computed through an optimization problem depending on probabilistic forecasts of the power and energy profiles. Adefarati and Bansal researched the environmental and economic benefits of using the diesel generator, the wind turbine generation system, the photo-voltaic system and the battery storage system in a microgrid system by using meteorological data [4]. Esther et al. [5] advocated the advantages of decentralized microgrid energy markets through a critical review of blockchain-based microgrid energy markets. An assessment of the potential wave energy is carried out based on a 30 year wind hindcast in [6]. The European Marine Energy Centre assessed the possible wave energy available around the globe [7]. Wave Energy Converters (WECs) are designed to extract the wave energy from the waves at a particular location [8,9]. A linear WEC has an effective and attractive technology, due to its reduced complexity. It enables the system to harvest energy directly from a buoy or a floater by ocean waves [10]. Thorburn et al. presented energy conversion from ocean waves to electricity with a focus on the transmission system in [11], and use case studies to investigate the various configurations. Leijon et al. [12,13] investigated the different renewable energy technologies in terms of economy and engineering solutions, by presenting the Degree of Utilization and defining how the concept is crucial for economic and design optimization. A grid-oriented approach for electricity production from ocean waves is reported in [14]. Due to the contrast between the load demand and the variable nature of the energy source, renewable energy generation alone is not sufficient to supply the load demand. To ensure a controlled power supply to the grid with an intermittent power source such as waves, standalone power systems rely on Energy Storage Systems (ESSs). At present, battery storage systems seem to provide a promising way of mitigating the issues of load demand and power generation fluctuations in most applications. However, they could increase the cost of the overall system because the batteries are short-lived because of the frequent charge and discharge cycles. Batteries have a high energy density but a low power density, i.e. low charge/discharge rates [15]. Supercapacitors (SCs) are a versatile form of energy storage, storing energy by means of static charge. Various effective ESS-based ways of controlling and power sharing have been proposed in [16].

1.1. Previous work on energy storage and control

Aneke et al. [17] gave a detailed analysis of different EES technologies, real-life application and performance of various EESs. Hassan et al. [18] reviewed the use of different energy storage technologies for wind energy systems, and Pires et al. [19] reviewed the various power converter interfaces for electrochemical energy sources. Literature reviews and studies provide an insight in using an EES to mitigate the inconsistency of renewable energy sources [20–22]. A rule-based control of a battery was proposed by Teleke et al. [23]. Zeng et al. and Hredzak et al. propose a simulation model for a battery energy storage

system and a model predictive control system for a hybrid battery-ultracapacitor power source [24,25]. A model predictive control system has the drawback that it requires extra mathematical computations which increase the computational cost. In [23,26], rule-based control schemes were proposed for an integration with the ESS, but the method requires substantial data storage and complex computations. Control strategies for smoothening the power by a power fluctuation rate limiter have merely been discussed. Mendis et al. [27] proposed the benefits of using a Hybrid Energy Storage System (HESS) for a wind-based system. Galvin et al. compared the performance matrix of batteries and supercapacitors [28]. A study for reducing the stress on the batteries by using SCs is proposed by Lahyani et al. [29]. Compared to batteries, SCs have a long life span (more than one million cycles) with a high-power density. Moreover, SCs provide a swift, and effective energy control [30]. Energy stabilization using SCs was demonstrated for intermittent renewable energy and fluctuating load applications in [31]. A crucial criterion for the selection of and the methods for storing the renewable energy is discussed in [32]. Greenwood et al. [33] investigated the feasibility and the impact of using an ESS for a frequency response by using an energy storage emulation. Dali et al. [34] investigated the operation of a hybrid Photo-voltaic and wind system to operate in parallel mode or in autonomous mode.

1.2. Motivation for this work

Different control strategies discussed in [35,36] and literature studies [37,38] promote the idea that an ESS is a suitable solution for the overall system efficiency improvement and the power smoothening of marine energy sources. Santos et al. [35] discussed the design and the implementation of a battery ESS operated with a three-phase bi-directional converter. The design provides a robust and energy efficient control and grid-integration of an ESS. Qian et al. [36] proposed a high-efficiency grid-tie battery-based ESS to mitigate the mismatch among the cells. Batteries, supercapacitors, flywheels etc. are the essential components for improving the power quality. The modeling and controlling of the components of an ESS effectively, the resulting system could benefit from (i) power quality improvement for intermittent power fluctuations, (ii) load leveling and peak shifting and (iii) system reliability [39,40]. In an application of harvesting wave energy, the DC-bus voltage is required to be constant at a desired value, which is higher than the voltages of a battery and a SC. A fully-active HESS topology is a suitable solution to achieve an effective control of the currents of the battery and the SC. However, both have individual characteristics in terms of energy and power density. Therefore, individual control is crucial for handling the power sharing between the battery and the SC, especially the control of their State-Of-Charge (SOC), so as to extend the life of the battery.

In this paper, we propose an energy management algorithm with a Dynamic Rate Limiter (DRL) function. This energy management control system (EMCS) addresses the problem of individual control effectively with a DRL. The EMCS decouples the low and the high-frequency power components and updates the power demand for the controllers of the battery and the SC. The DRL updates the power demand to the battery controller to regulate the SOC within the allowed limits. This algorithm, collectively, generates an updated demand value for the HESS to store and generate the required power and controls the SOCs. This topology is compared with well-known topologies to show the practicability of the work. The comparison shows the current profiles and the energy losses for individual topologies. The proposed control provides an effective and individual current control for both power sources using the DC/DC converters. The control protects the battery from high transients and reduces the losses, which ensures a longer battery life. As the SC is a high-power density source, it can handle the high-frequency power components and reduce the stress on the battery. Hence, the overall maintenance and the cost of the system can be reduced.

The remainder of this paper is structured as follows: Section 2 contains a description of the wave energy-park and the HESS system. In Section 3, control modeling is described and followed by the sizing of the HESS, the control topology and the analysis of the critical bandwidth; in Section 4 the results and the analysis of the proposed control method are presented and discussed. Section 5 gives the conclusions of the study and a suggestion for the future work.

2. System description: Model and the power flow

In this study, we consider a Wave Energy Park (WEP) as the power source. Each WEC consists of a surface buoy connected to a linear generator moored with a foundation on the seabed, and are based on the WEC concept developed by Uppsala University, which have been installed offshore at the Lysekil test site [8,41]. Thorburn et al. [42] presented the results from a small-scale farm for the varying position of the translator in a linear generator. Experimental studies of a linear generator based WEC for the power absorption at various load cases and an improved power to the DC bus have been carried out at the Lysekil wave research site [43,44]. The time-series of the irregular waves used as input data for the wave energy park model, were measured offshore at the Lysekil test site [45]. Waves are varying in nature and generate power of varying amplitude and frequency. When the total power from the WECs is higher than the demand of the grid/loads, the SC stores the excess amount of power in parallel with the battery. This dual combination of power-sharing feeds the power to the DC-link to meet a power demand when the WECs are not producing sufficient power and stores the excessive power if the WECs are producing more than the demand. This combination saves the battery life by avoiding the fast charge and discharge cycles. The HESS is interfaced at the DC-link (an appropriate point of connection of an EES) with the local grid to address the problem of power bridging. The proposed system with hybrid energy storage is shown in Fig. 1.

2.1. Introduction to the wave energy park model

In the procedure of harvesting energy from the waves, it is necessary to have knowledge of the park site in order to design and tune the WECs.

The layout of the park is given in detail in [46]. The hydrodynamic modeling of the wave energy park is carried out with an analytical method based on multiple scattering theory. The method has been verified against the benchmark software WAMIT and used to study the optimization of large wave energy parks in [45,46]. The power absorbed from the WECs is presented in Fig. 2. Each curve represents the power of individual WEC placed in the park. The total power from the park is the sum of power from each individual WEC in Fig. 3. These data are used as input for the model in order to study the behavior of the

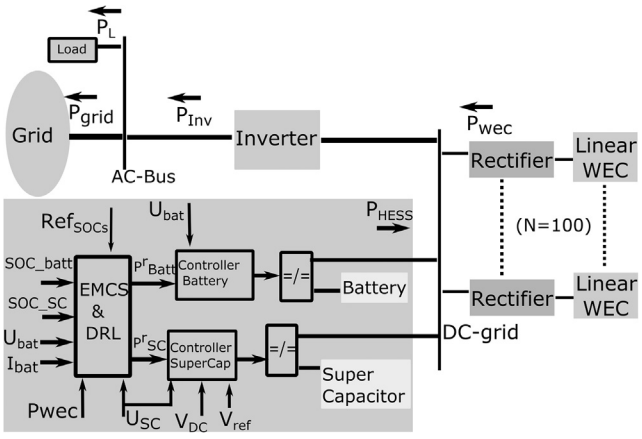

Fig. 1. Hybrid energy storage system connected with WEP and AC-grid.

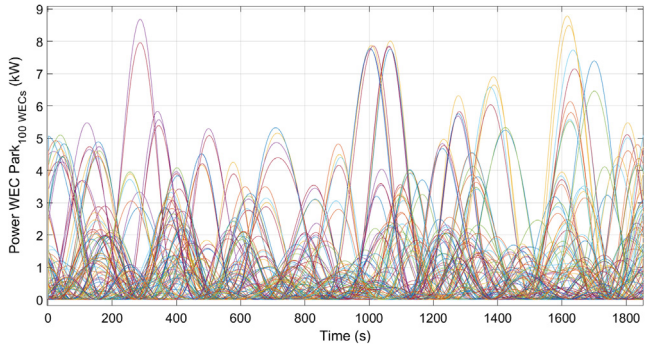

Fig. 2. Each curve represents the power absorbed by an individual WEC.

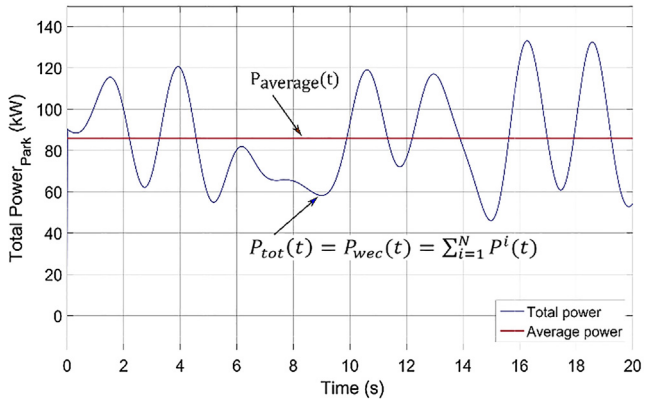

Fig. 3. WEP electrical power and average power for an observed period of 20 s.

HESS with the proposed strategy.

The aim is to minimize the power fluctuations and to improve the power quality to the grid by keeping a steady power output from the inverter ($P_{inv}(t)$). The HESS exchanges the power ($P_{HESS}(t)$) which is a difference of power produced by the WECs based wave energy park, ($P_{WEC}(t)$) and the power exchanged with the local AC-grid ($P_{grid}(t)$). The AC power from the WECs is converted to DC power and fed to the DC-grid. The AC-grid power ($P_{grid}(t)$) is considered as an average power component ($P_{average}(t)$) of the power generated by the park. The power and the size of the HESS are calculated [47,48] in Eq. (1) and Section 3.2 respectively. The total and the average power from the park are shown in Fig. 3.

$$P_{HESS}(t) = P_{WEC}(t) - P_{inv}(t) \tag{1}$$

$$P_{HESS}(t) = P_{WEC}(t) - P_{grid}(t) \tag{2}$$

Since the power from the park is varying in time, the power from the inverter should be kept steady to minimize the fluctuations for a considered time interval. A second-order Low Pass Filter (LPF) is used to separate the low-frequency component from the total power ($P_{WEC}(t)$) of the WEP.

3. Control modeling methodology

3.1. Modeling of the energy management control system

The energy management control system generates a power demand command for the controllers of the batteries and the SC in order to reduce the excessive stress on the battery and meet the power demand at the DC-grid.

The EMCS updates the demand continuously with DRL and commands the controllers to generate a reference current. The EMCS decouples the high-frequency and the low-frequency power fluctuations and generates a new demand to the DC/DC controllers. The low-frequency power components are shared by the battery while the high-frequency components are effectively addressed by the SC due to its high power density characteristic. Eqs. (1) and (2) generate a value as a power demand, $P_{HESS}(t)$, to maintain the average power injected into the grid. In this way, the sharing of the power components is controlled by the EMCS. This control algorithm is based on the measured and referenced SOCs of the battery, the SC and the power demand. The EMCS updates the power demand value for the battery and the SC by keeping the SOCs in the allowed range. An updated demand value controls the DC/DC converter by updating the command to charge and discharge the HESS components. The DRL takes action when the SOC of the battery breaks the upper or the lower limits set for the battery. The rate of power change at time t provides an initial power of the battery of the HESS, and can be obtained from Eq. (3).

$$r_{batt}(t) = \frac{P_{\overline{HESS}}(t) - P_{\overline{HESS}}(t-\Delta t)}{\Delta t} \tag{3}$$

where $r_{batt}(t)$ is the rate of the power change for the battery, and $P_{\overline{HESS}}(t)$ is the filtered variable of the power component to be addressed by the battery. This combination of the DRL with the EMCS generates a new power demand for the HESS and is calculated for the battery and the SC by Eq. (4).

$$P^{new}_{HESS}(t) = P^{r}_{SC}(\Delta t) + P^{r}_{Batt}(\Delta t) \tag{4}$$

where $P^{r}_{SC}(\Delta t)$ and $P^{r}_{Batt}(\Delta t)$ are the updated power demand for the SC and the battery controller command units. The change in each time iteration is Δt. $P^{r}_{Batt}(\Delta t)$depends on $P_{Batt}(t)$ and ΔP_{Batt}, the latter is the DRL-power based on Eq. (7). The rise and fall rate limiter, α^{rise}_{batt} and α^{fall}_{batt}, for the three cases are discussed later in this section. The rise and fall rate limits are calculated as in Eq. (5).

$$\left.\begin{aligned} \alpha^{rise}_{batt} &= \frac{P^{rated}_{HESS} \cdot d_{batt}}{T} \\ \alpha^{fall}_{batt} &= -\frac{P^{rated}_{HESS} \cdot d_{batt}}{T} \end{aligned}\right\} \tag{5}$$

P^{rated}_{HESS} is the rated power of the HESS, d_{batt} is the allowed power fluctuation for the battery for a considered time period T. d_{batt} is considered as 10% for the 6 s.

$$P^{r}_{Batt}(\Delta t) = P_{Batt}(t) + \Delta P_{Batt} \tag{6}$$

$$\left.\begin{aligned} \Delta P_{Batt} &\propto \delta_i \cdot v_{Batt} \\ \Delta P_{Batt} &= \rho_i \cdot \delta_i \cdot v_{Batt} \end{aligned}\right\} \tag{7}$$

$$\delta_i = \frac{SOC_m - SOC_{ref}}{\left(\frac{SOC^{max} - SOC^{min}}{2}\right)} \tag{8}$$

where $P_{Batt}(t)$ is the power command generated by the EMCS based on Eq. (1) after decoupling the low-frequency and the high-frequency power components, SOC_m and SOC_{ref} are the measured and referenced values of the battery SOC, δ_i is the SOC function which controls theΔP_{Batt} to update a demand power command for the batteries. ρ_i is the variable accelerator for giving an effect to the δ_i to avoid the upper and lower limits of the SOC. The variable, ρ_i is treated as a power factor which is based on a look-up table defined for the allowed ranges of the SOC for the battery and the SC. The cases for the rate limiter function are as follows:

(a)$\alpha^{fall}_{batt} \le r_{batt}(t) \le \alpha^{rise}_{batt}\Delta P_{Batt}$ remains zero for this case when the SOCs are in the allowed limits. ρ_i is kept zero for the acceptable fluctuating range of the SOC. Hence Eq. (6) yields into Eq. (9),

$$P^{r}_{Batt}(\Delta t) = P_{Batt}(t) \tag{9}$$

(b)$r_{batt}(t) > \alpha^{rise}_{batt}$

Then the updated power demand

$$P^{r}_{Batt}(\Delta t) = P_{Batt}(t) + \Delta P_{Batt} \tag{10}$$

ΔP_{Batt} value will be a positive factor. This will give a rise to the new

power demand value to keep the SOC within the allowed limits.

(c) $r_{batt}(t) < \alpha_{batt}^{fall}$

$$P_{Batt}^{r}(\Delta t) = P_{Batt}(t) - \Delta P_{Batt} \tag{11}$$

Then, ΔP_{Batt} will be negatively amplified and will decrease the power demand to control the SOC of the battery.

The EMCS ensures a balanced power distribution between the battery and the SC. If SOC_{ref}^{SC} of the SC has a fluctuation in the allowed SOC range then most of the power distributions are shared by the SC and only a few low-frequency power components are shared with the battery. The updated power demands are used in the control strategies to compute a new power demand $P_{HESS}^{new}(t)$ for the HESS.

3.2. Dimensioning of the battery and the supercapacitor

In order to reduce the power fluctuations, and the stress on the battery and as well as achieve a steady state range for the SOCs, $P_{inv}(t)$ should be kept constant for an observed time interval (T_w). Therefore, the battery and SC-based HESS configuration should be chosen correctly. The energy in the HESS can be determined as Eqs. (12) and (13) gives a close estimation of the maximum power of the HESS. The grid power is the average power of $P_{WEC}(t)$ for $T_w = 20$ s.

$$E_{HESS}(T_w) - E_{HESS}(0) = \int_0^{Tw} (P_{WEC}(t) - P_{inv}(t))dt \tag{12}$$

$$P_{HESS,max} = max\ |P_{WEC}(t)|_{T_w} - P_{grid}(t)_{T_w} \tag{13}$$

Therefore, the sizing of the HESS is based on the $E_{HESS,max}$ for a specific time period. This consideration matches the power requirement and computes a maximum power for the HESS.

In this study, the maximum power of the WEP, where each WEC is scaled to 10 kW only, is 137 kW and the average power is 86 kW for a time period of 20 s, as shown in Fig. 3. Eq. (13) gives a close estimation of the maximum power of the HESS, $P_{HESS,max} = 137\ \text{kW} - 86\ \text{kW} = 51\ \text{kW}$. The energy rating of the HESS from Eq. (12) is 104.125 kJ, shown in Fig. 4, which is a difference of time integral for the power profiles (maximum and minimum) of the WEP and the average power, to be shared with the AC-grid. The selected SC pack is 66 kW, 30% higher than 51 kW, to accommodate for any degradation over time. A battery pack of 28 kW is connected in parallel with the SC. The parameters of HESS are given in Table 1. By converting Joule to kWh ($1\text{J} = 2.28e^{-7}$ kWh), 104 kJ gives 27.8 Wh of energy rating for the HESS. The peak energy content of SC and battery is 48 Wh and 20 kWh. The adopted size of the HESS compensates the power and ensures a steady power, $P_{inv}(t)$, for a considered time interval.

The SC has feasible advantages over the battery because of its large power-density [48]. Hence the energy can be withdrawn much faster than from the battery. Due to this effect, the battery and the SC yields different transients behavior of their currents, which are discussed with a bandwidth analysis in Section 3.3.2.

3.3. Hybrid control topology

Several HESS control topologies have been proposed in the literature and used in various applications [49,50]. The HESS can be configured in different topologies in order to control the power flow between the battery and supercapacitor. Battery and SC based HESS topologies can be categorized into three main categories. The passive topology, semi-active topology and fully-active topology are the best known methodologies for controlling the power sharing among HESS elements as shown in Fig. 5. For a passive topology, the terminals of the battery and the SC are directly interfaced with the DC-link and the power sharing and the response are determined by the characteristics of the individual HESS elements, as in Fig. 5(a). A passive topology is a simple and easy way to power flow, where battery and SC are connected to the DC-link without any control. In this topology, the power distribution is limited by the internal resistance and causes an inefficient control [51].

In this topology, the active component as a bi-directional DC/DC power converter is not used, thus the large capacity of the SC cannot be exploited fully. Because of this drawback, the passive topology is not used in real-applications [50,52].

Semi-active topologies have been proposed to exploit the mutual benefits of the passive and the active HESS elements, as shown in Fig. 5(b) and (c) [53]. A semi-active topology, in which only one DC/DC converter is connected to the battery or the SC [54], might be a good trade-off in terms of cost saving and power-sharing and could be used in some applications [55]. However, the SOCs could merely be controlled together but not individually, due to the lack of control for charging and discharging each unit [56].

For the battery semi-active topology, the battery is controlled by a DC/DC bi-directional converter, while the SC is directly connected with the DC-link in a passive mode as shown in Fig. 5(b). This topology does not provide a suitable stability in the DC-link voltage due to the linear voltage-capacity characteristics. The low volumetric-efficiency of the SC capacity-usage is the major drawback of this topology and requires a secured installation of the SC to handle the DC-bus voltage variation [57]. Conversely, the SC semi-active topology interfaces the SC with the bi-directional DC/DC converter and passively connects the battery with the DC-link. In this topology, the control allows the terminal voltage of the SC to vary in a wide range which improves the volumetric-efficiency [53]. However a high efficiency DC/DC converter should be used to improve the overall efficiency of the HESS [58].

In a fully-active topology, the HESS components employ bi-directional DC/DC converter. This configuration isolates the individual elements from the DC-link and allows an active control of the power flow among individual HESS elements as in Fig. 5(d). The parallel fully-active topology presents a good control effect which allows a control of the power flow by individual bi-directional DC/DC converter connected to the battery and the SC. The HESS components run at different terminal voltages while regulating the DC-link voltage with less losses over the HESS. Because of this advantage, various energy management control algorithms have been proposed and developed aiming to reduce the stress on the battery and improve the overall system efficiency [25,55,59].

In this study, a parallel fully active topology is deployed with an improved EMCS and proposed a DRL function. In the proposed control the power from the WEP is interfaced with a DC-link having a capacitor in parallel with the HESS Fig. 1. This configuration forms a DC microgrid, operating at 790 V magnitude. This is interfaced with a three-phase AC-grid by a voltage source inverter (VSI) followed by a harmonic filter. VSI transfers the active power to the grid and minimizes

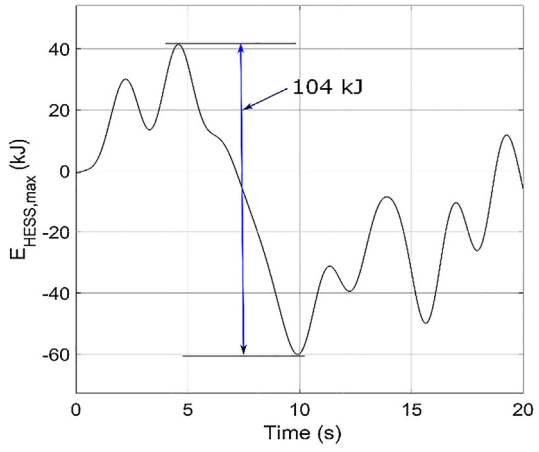

Fig. 4. Energy profile for the HESS maximum power estimation.

Table 1
Parameters for the supercapacitor module and the battery pack.

Parameter	Supercapacitor parameters	Battery-pack parameters
Rated voltage	380 V	340 V
Rated capacity	2.4F	60 Ah
Rated power[a]	66 kW	28.5 kW
Number of cells Cell capacitance	144 (2.7 V each) 350F	96 (3.6 V each) 60 Ah

[a] Estimated [48], (characteristics of EES systems [20,21]).

the current distortion. The DC-link voltage is kept steady by the HESS.

In this paper, we propose an EMCS and DRL based fully active HESS topology, shown in Fig. 6, based on two bidirectional DC/DC converters to decouple the hybrid power system between the battery and the supercapacitor. This topology provides an individual control for both power sources through the DC/DC converters. This topology is an efficient, stable, and flexible way for power distribution between the battery and SC. It protects the battery during the transient process by limiting high current bursts, which prolongs the battery life. The control strategy depends on the status of the power demand, $P_{HESS}(t)$, given in (1). A positive $P_{HESS}(t)$ defines an excess amount of power which is higher than the power required by the local AC-grid or the load. This extra power is stored in the batteries and the SC. In this mode of operation, DC/DC converter acts in the buck mode and absorbs the extra power from the WEP via the DC-link. A negative value of the $P_{HESS}(t)$ changes the mode of operation to boost mode. The control mode of DC/DC converter depends on the status of the SOC of the battery and the SC. This control effectively adjusts the SOCs to the allowed ranges by changing the mode of the DC/DC converter even if the $P_{HESS}(t)$ is positive. This ensures the power demand to be met by the HESS and reduces the dynamic stress and losses, hence increasing the battery life.

3.3.1. Control strategy of the batteries and supercapacitors based HESS

In this study, two bi-directional DC/DC converters are used in buck-boost mode, controlled by the EMCS and the DRL as seen in Fig. 6. The main objectives of this control strategy are:

- To reduce the stress on the battery and increase the lifetime.
- Continuously update the power demand and control the SOCs of the battery and the SC.
- Supply a smoothened average power to the local grid.

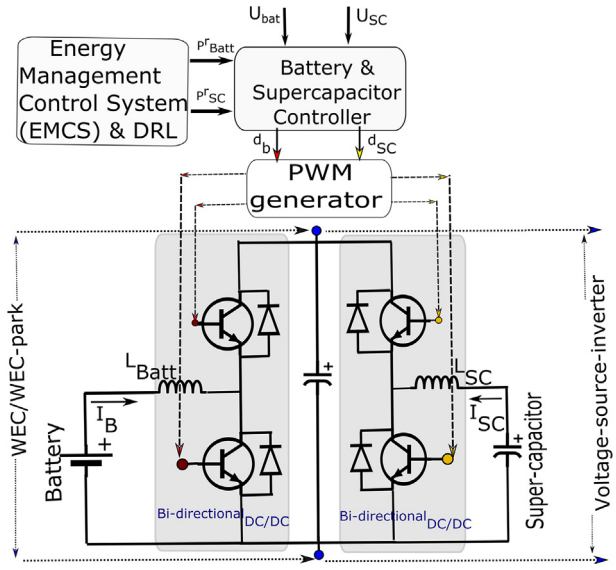

Fig. 6. A fully-active HESS control topology.

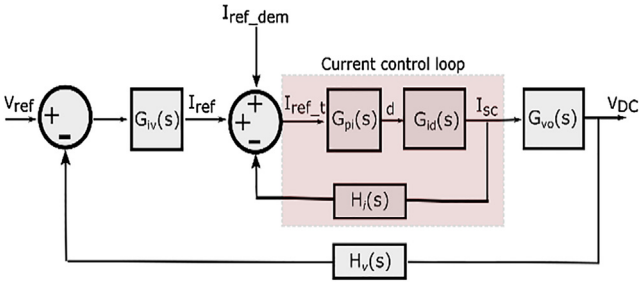

Fig. 7. Block diagram of supercapacitor controller.

Fig. 7 shows a block diagram for an interfaced controller for the SC. This control has two parallel loops to control the DC-link voltage, the outer loop, and the inductor current, the inner loop. The DC-link voltage is kept steady by this control scheme. A feedback voltage signal V_{DC} is compared with the referenced voltage signal V_{ref} and an error is fed to a Proportional-Integral (PI) controller. This PI controller generates a referenced current which is compared with the instant inductor current

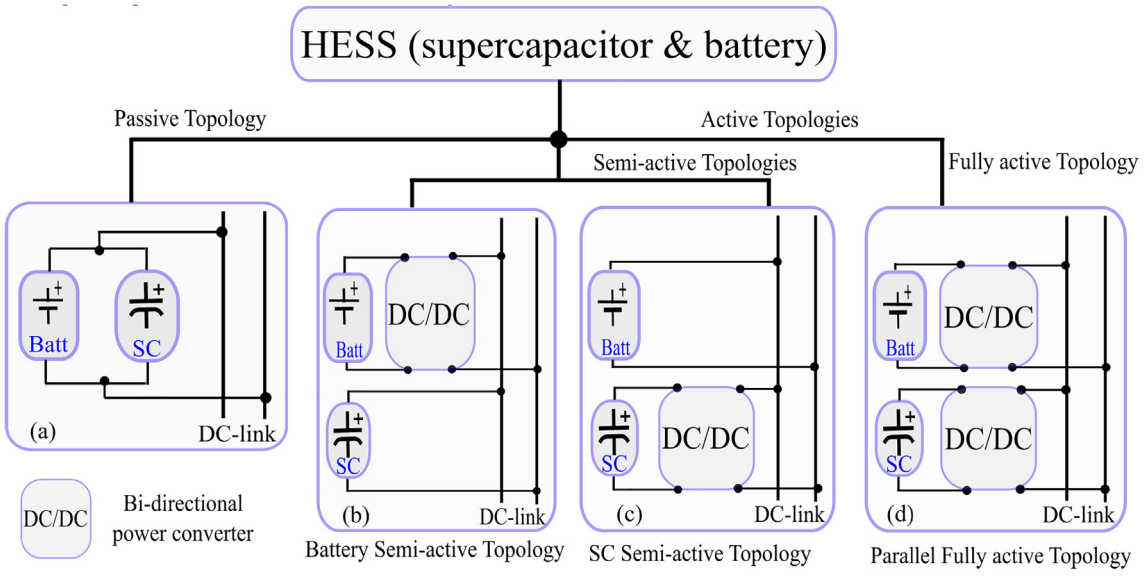

Fig. 5. A classification of well-known HESS control topologies.

and a referenced demand current, i_{ref_dem}, to generate an error signal to the PI controller. The error signal is adjusted and generates a duty ratio, d, to the Pulse Width Modulator (PWM) to generate pulses to control the inductor current.

The SC and the inductor are connected in series, which allow current flow from the SC to regulate the DC-grid voltage to a constant level. If the measured value of V_{DC} is higher than the referenced value V_{ref}, the SC is switched to operate in buck-mode to store the extra energy. Hence, DC grid voltage is controlled to rise. If the V_{DC} is lower than the V_{ref} the controller acts in boost mode to supply energy to keep the DC-grid stable. A separate control for the battery connected with the DC-link through the DC/DC bidirectional converter is shown in Fig. 8. The referenced current, i_{ref_batt}, for the battery is obtained to control the current demand based upon the updated power demand and the SOCs of the battery and the SC. The signal i_{ref_batt}, is based on the low frequency power demand component generated by the EMCS.

3.3.2. Controller design for a hybrid energy storage system: Bandwidth analysis

A HESS based system is a composite unit of a battery and a SC. Each unit has an individual control and exhibits a different behavior, which is based on the loop Bandwidth (BW) of the controllers. The SC presents a faster dynamic for charging and discharging compared to the battery. Therefore, the BW analysis of the controller becomes a vital point to verify the controller's design for a smooth and reliable operation. A bidirectional DC/DC converter uses the same transfer function for the buck and boost mode [60]. The current control loops for the battery and the SC designed according to their dynamics behavior based upon the switching frequency, $f_{sw} = 10$ kHz. The SC has an outer loop for voltage control and an inner loop for current control. The SC inner current loop is limited to $f_{sw}/6$. This loop can handle fast transient changes effectively. Due to the slower dynamic of the battery, the current control loop has to be slower than the SC current loop. Therefore, the BW for the battery current loop is kept at $f_{sw}/10$ [61].

This criterion of BW selection avoids the subharmonics oscillations and benefits the stability of the system by ensuring the diversion of faster dynamics to the SC. The voltage loop BW is kept slower than the inner current loop of the SC. A total referenced current, i_{ref_t}, is generated and given to the current control loop. This total referenced current is defined in Eq. (14).

$$i_{ref_t} = i_{ref} + i_{ref_dem} - i_{SC} \tag{14}$$

A transfer function of the control to the inductor current is obtained [62,63] in Eq. (15).

$$G_{id}(s) = \frac{\bar{I}_L}{\bar{d}} = \frac{V_{DC}Cs + 2\frac{V_{DC}}{R}}{LCs^2 + \left(\frac{L}{R}\right)s + (1-d)^2} \tag{15}$$

where $I_{sc}$is the inductor current which is mentioned as I_L in (15). The open loop transfer function for the current control loop compensator is given by Eq. (16).

$$G_{ol}(s) = G_{pi}(s)G_{id}(s)H_i(s) \tag{16}$$

$G_{pi}(s)$ is the transfer function for the PI compensator and defined in Eq. (17).

$$G_{pi}(s) = K_{p,sc} + \frac{K_{i,sc}}{s} \tag{17}$$

The Bode plot of the open-loop transfer function is shown in Fig. 9 based on the nominal parameters and the parameters available in Table 2. The battery internal resistancer_{ib}, the inductor parasitic resistance R_{lp} and the turn-on resistance R_{on} are also included in this study and yields a parasitic resistance, r_p. The additional parameters used in Simulink are reported in Table 3.

The blue line in the Fig. 9 presents the behavior of current control loop with gain and the red-line entails a response without gain. It can be noted that the system provides a phase margin (PM) of 90° at 14.3 krad/s (2.3 kHz) as a crossover frequency, f_c. This, indeed, is a good indicator for addressing the very high frequency components by the SC when a large PM is required. In our application, the PM requirement is not this large. Therefore the controller needs a design to operate at a new crossover frequency of $f_{sw}/6$ with a phase margin lower than 90°. In this way, it can address the low-frequency power components faster as well. To this end, one pole and one zero have to be placed in the appropriate positions. Before assigning the positions of the pole-zero pair, one pole is situated at $f_{sw} = 10$ kHz and one zero is below the minimum crossover frequency, $f_c/2$. The requirement for a stable system is to fix the BW at $f_c = f_{sw}/6 = 1667$ Hz (10.04 krad/s). This is achieved by placing one zero at $f_c/2 = 833$ Hz. To eliminate the noise spikes, one pole is placed at$6f_c/2 = 5$ kHz (31.4 krad/s). This combination reduces the PM to 60° (approximately) and provides stability to the system. The aforementioned requirement is achieved by designing the control parameters in a Single Input Single Output (SISO) tool in MATLAB. The parameters for the SC are given in Table 1.

The Bode plots in Fig. 10 show two response curves, the blue response is a new crossover frequency after having tuned the PI controller in the SISO tool at $f_c = f_{sw}/6(10.01$ krad/s) with a reduced PM of 60°. The yellow line shows the response of previous PI controller as a comparison. The PI controller tuned parameters are $K_{p,sc} = 0.212$ and $K_{i,sc} = 634$. A transfer function of control to the inductor current for the battery control loop is given in Eq. (18) [62,63]. Fig. 11 presents the Bode plot of the current control loop for the battery controller with the compensator and without a compensator. The open loop transfer function of the current controller and the transfer function of the open loop compensates for the battery controller are presented in

$$G_{id_b}(s) = \frac{V_{DC}Cs + 2\frac{V_{DC}}{R}}{L_bCs^2 + \left(\frac{L_b}{R}\right)s + (1-d_b)^2} \tag{18}$$

Eqs. (19) and (20). The PI compensator is designed to address the low-frequency power component and to divert the frequent transients to the SC. These criteria advocate to set a lower BW of the control loop than the selected BW of the SC current control loop.

$$G_{ol_b}(s) = G_{pi_b}(s)G_{id_b}(s)H_{i_b}(s) \tag{19}$$

$$G_{pi_b}(s) = K_{p,b} + \frac{K_{i,b}}{s} \tag{20}$$

Since the SC current loop BW is set to$f_c = f_{sw}/6$, a lower limit BW is kept at $f_{cb} = f_{sw}/10$ (6.31 krad/s) for the battery current loop. The PI compensator gains are calculated at $K_{p,b} = 0.021$ and $K_{i,b} = 6.24$ for a stable control.

In Fig. 11, the PI controller is designed to achieve a phase margin of 60° at the cut-off frequency, 6.31 krad/s. The specific parameters of the battery pack, the SC and the parameters of the converters considered for this simulation study are given in Tables 1 and 2, respectively. The battery pack consists of Lithium-Ion (Li-ion) batteries for the HESS topologies under the investigation.

4. Results and discussion

In this section, the applicability of the proposed strategy is verified by the simulation results carried out in the MATLAB/Simulink environment. The simulations were conducted for different HESS

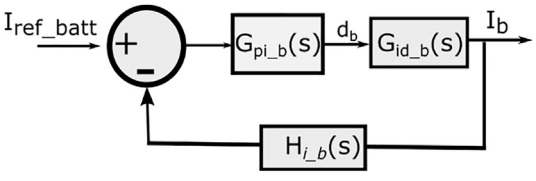

Fig. 8. Block diagram of the current controller of the battery.

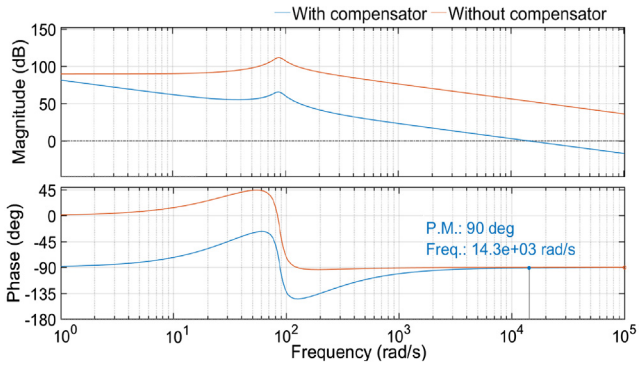

Fig. 9. The Bode plot for the SC current control loop.

Table 2
DC-grid parameters used in the simulation study.

Parameter	Symbol	Value
DC-voltage	V_{DC}	790 V
DC-grid-capacitor	C	5000 μF
DC-grid- resistance	$R = V_{DC}/I_{dc}$	33 Ω (virtual)
DC/DC-converter-inductance (SC, Bat.)	L	1.80 mH
	L_b	2.23 mH
Duty ratio (SC, Bat.)	d, d_b	0.37, 0.5
Inductor resistance	R_{lp}	0.04 Ω
Turn-on resistance	R_{on}	0.016 Ω
Parasitic resistance	$r_p = R_{lp} + R_{on}$	0.056 Ω
Battery resistance	r_{ib}	0.06 Ω

Table 3
Additional parameters utilized in Simulink.

Electrical characteristics (WEC)	Value	Parameters	Value
Synchronous inductance	21.2 mH	Grid voltage	400 V
Winding resistance	0.36 Ω	Grid frequency	50 Hz
Rated armature current	40 A	Inverter power	120 kVA
Rated power	20 kW	HESS power	80 kW
Rated voltage	450 V	DC/DC-converter (*Psc - rated power*)	50 kW
Nominal speed	0.7 m/s	DC/DC-converter (*Pb - rated power*)	30 kW

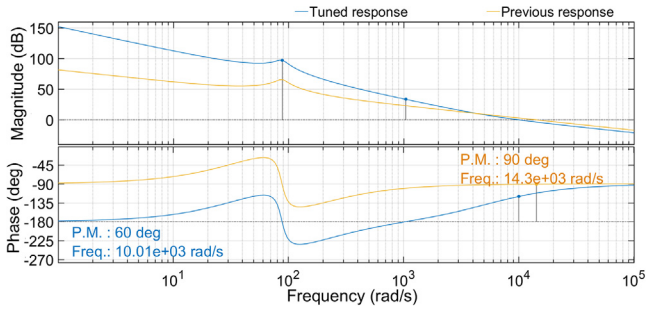

Fig. 10. The Bode plot of the current control loop of SC at new crossover frequency 10 krad/s.

interfacing well known methodologies and compared to the proposed control in order to verify the vulnerability for real applications. Four different HESS interfacing topologies are studied: (1) The passive HESS, (2) The battery semi-active HESS, (3) The SC semi-active HESS and (4) the conventional fully-active HESS topology as classified in Fig. 5. The simulations were performed for 20 s each. The model parameters are kept identical during the simulations in order to present a comparison and tabulated in Tables 1 and 2.

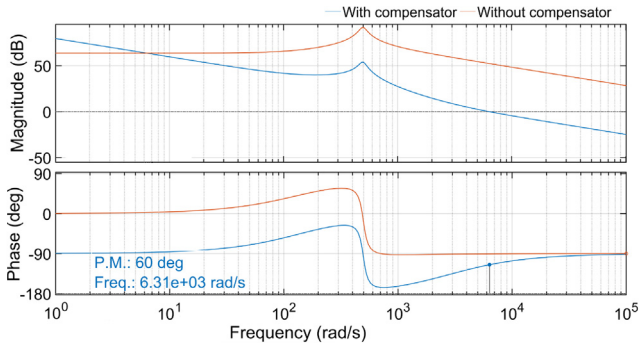

Fig. 11. The Bode plot of the current control loop of the battery.

4.1. Comparison of different HESS topologies

The different HESS topologies current profiles are presented with their respective energy losses in Fig. 12. Fig. 13 shows the difference of the proposed control compared to known topologies to prolong the battery life. The graphs on the left (Fig. 12(a), (c), (e), (g)) show the current profiles for the battery (blue line), the SC (red line) and the demand current (cyan line) in different HESS interfaces while the graphs on the right side, present the reported energy losses during the simulations in different HESS topologies.

In the passive topology, both the SC and the battery compensate for the fluctuations by absorbing and releasing the energy. The power sharing capabilities of passive HESS depends on the internal parameters of the battery and the SC. Therefore, the power sharing is limited in this topology and a poor efficiency is expected for an intermittent power source or a varying load situation. The battery is modeled as a constant voltage source with an equivalent series resistance, and the SC model uses a large capacitance with equivalent series resistance. Fig. 12(a) and (b) clearly show the poor performance of passive HESS for an intermittent power source. The current profiles of battery and SC have large fluctuations and barely meet the current demand with higher energy losses on the HESS components. Due to this lack of control, this topology is not relevant for a real application. Fig. 12(c) and (d) present the current sharing between the battery and the SC with their energy losses for a battery semi-active topology. The Simulink model for this topology is modeled with similar parameters as the previous topology. Firstly, the $P_{HESS}(t)$ is filtered by a LPF filter to decouple the high and low frequency fluctuations. A time constant ($\tau = 0.35$ s) is set for the LPF and can be altered to meet the use of the battery. The low frequency components are addressed by the battery with a DC/DC converter while the SC is directly interfaced with the DC-link. A simple PI controller is used for the current tracking and the rest of the current sharing is handled by the passively connected SC. A low bandwidth is tuned for the PI controller to achieve a smoothness in the battery current while the SC capacity is kept larger. In Fig. 12(c) & (d), the battery shares less fluctuating components while the SC covers wider range of fluctuations. Hence, a large energy loss is reported on the SC module while the battery with the converter has lower losses. The total HESS losses are ranging to 400 kJ due to the higher fluctuations on the SC. Comparing Fig. 12(b) to the Fig. 12(d), where the total loss is higher than 500 kJ, shows a significant improvement in the battery current profile. However, the total HESS losses have not improved much in this control topology. Conversely, the SC semi-active topology shows an improvement in the SC current profile and slightly higher losses in the battery module as shown in Fig. 12(e) and (f). This improvement is caused by the time constant of the LPF which is kept identical in the Simulink model. However, the time constant can be adjusted to share more current by the SC. This power sharing setting would increase the losses of the SC due to the rapid functioning of the DC/DC converter. In this setting, the converter would take more action to handle the demand current and hence higher losses would be expected. The total

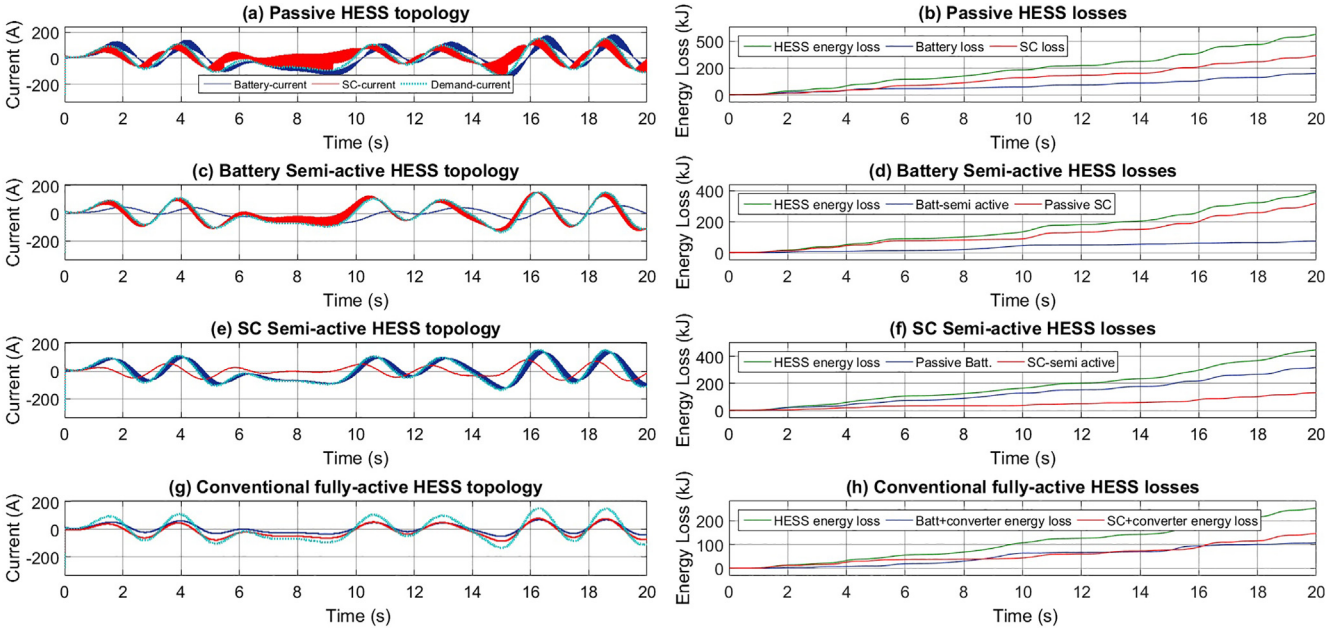

Fig. 12. Simulated current profiles of different HESS topologies and respective energy losses.

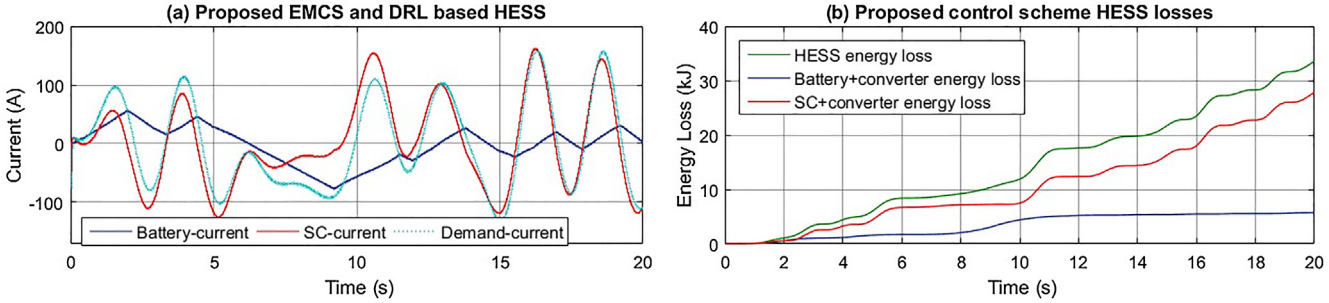

Fig. 13. Simulated current profiles and energy losses of the proposed EMCS and DRL based HESS control scheme.

HESS losses would be virtually identical to the previous topology. This topology has the benefit of a SC capacity use by isolating the SC from the DC-link which results in an improved volumetric efficiency. Therefore the DC/DC converter efficiency should be chosen higher to compensate for the losses difference. The power flow of the SC module is controlled by the duty cycle generated by the PWM which is a resulting action on the net change in the measured current.

A fully-active HESS topology is depicted in Fig. 5(d) where both the HESS components use a bi-directional DC/DC converter and share the power to meet the demand. For a conventional fully-active HESS topology, the power demand is passed through an LPF to decouple the high-frequency and the low frequency components. The high-frequency component and the filtered component are used as a reference signal to control the power flow for the SC and the battery module, respectively. This topology controls the individual power flow and reduces the energy losses of the HESS components significantly. However, the cost of the system increases with an increase of HESS components if the rating is not evaluated carefully. Fig. 12(g) and (h) show the current profiles and the losses of a fully-active HESS. Compared to the previous topology, the total HESS losses have been reduced up to 50%. The battery losses are reduced to 100 kJ (reduced to 40%) as shown in Fig. 12(h) but this can be improved further by adopting an improved energy management control system.

4.2. Simulation verification of the proposed control algorithm

In order to maximize the benefits of the previous topologies, this study proposes an EMCS with a DRL function to improve the control of the fully-active topology. The proposed control aims to reduce the battery losses and prolong the battery life. The proposed control topology is explained in detail in Section 3 and Fig. 13(a) and (b) present the current profiles and greatly reduced losses of the HESS components. The total HESS losses obtained from the proposed control are reduced to 80% of the conventional fully-active topology. The losses of the battery module have been reduced to a great extent and the SC losses are reduced to 75% compared with Fig. 12(h). The current profiles in Fig. 13(a) show that the power sharing of the HESS components justifies the proposed control algorithm. The battery current is significantly improved and the results report that the losses are reduced to a significant level, especially, of the battery module. It can be noted that the reduced losses in the battery module would increase the battery life and the overall cost can be reduced. Hence, this control can be implemented to applications harvesting wind, photo-voltaic and wave energy by extracting the required energy content from the power profiles of the renewable energy resources as in Eq. (1).

The power from the WEP is interfaced at the DC-link and the smoothened average power is injected into the AC-grid for the observed time period of 20 s as shown in Fig. 14(a). The average power of the wave energy park is delivered to the grid via the inverter while the fluctuating components are addressed by the HESS to optimize the power quality. Fig. 14(b) presents the frequency at the point of common coupling (PCC). The frequency deviation is fairly controlled under the m-Hz range. This control is not discussed in this paper. Since this study covers the grid-connected system, it is crucial to control the frequency

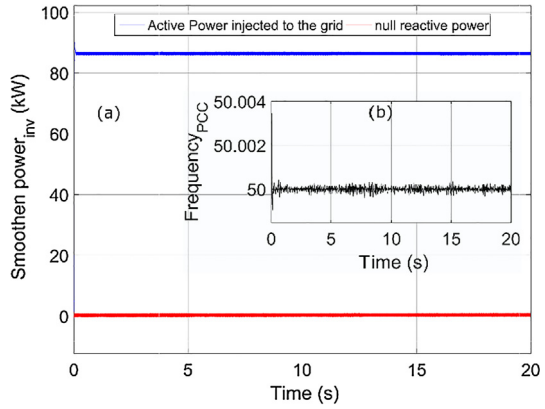

Fig. 14. (a) Steady inverter power $P_{inv}(t)$ injected into the local AC-grid with unity power factor. (b) Frequency at the PCC.

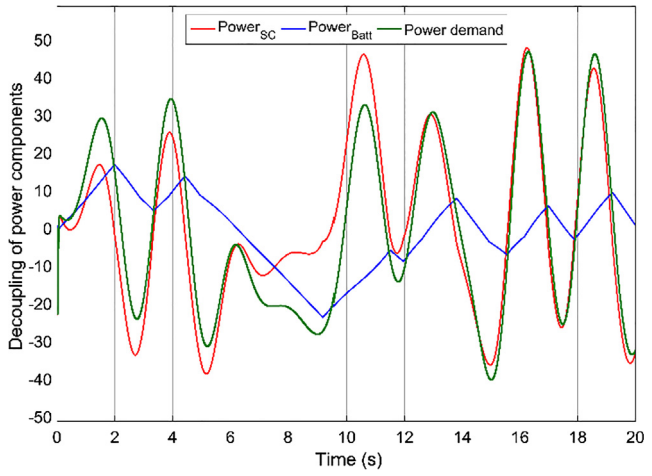

Fig. 15. Decoupled and updated power components from EMCS and DRL.

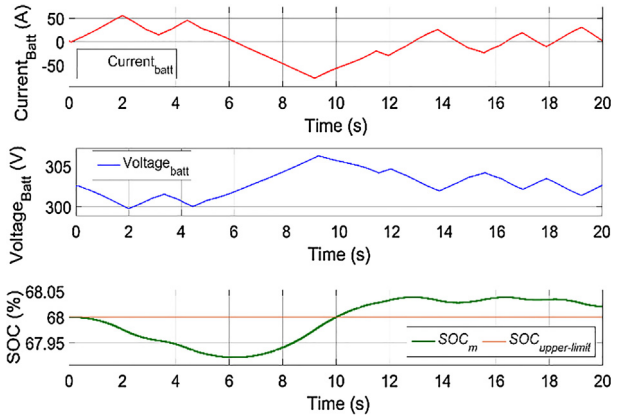

Fig. 17. Performance of the battery presented with the electrical quantities.

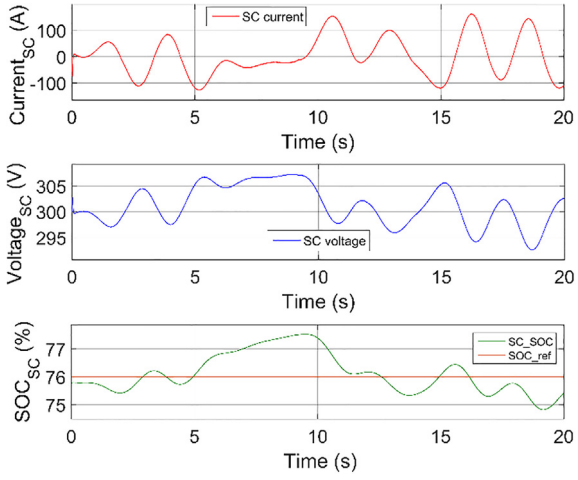

Fig. 18. Performance of the SC presented with the electrical quantities.

at the PCC within the allowed range specified by the grid code. In order to verify the control strategy, the numerical results are presented in Figs. 15–20. The EMCS decouples the high-frequency and the low-frequency power components and generates an updated power demand with and without DRL for the HESS. Fig. 15 presents the decoupled power components (Eq. (4)) to be addressed by the HESS in order to meet the power demand (Eqs. (1) and (2)) by storing and supplying the power to maintain a constant DC-link. The power demand is simply the

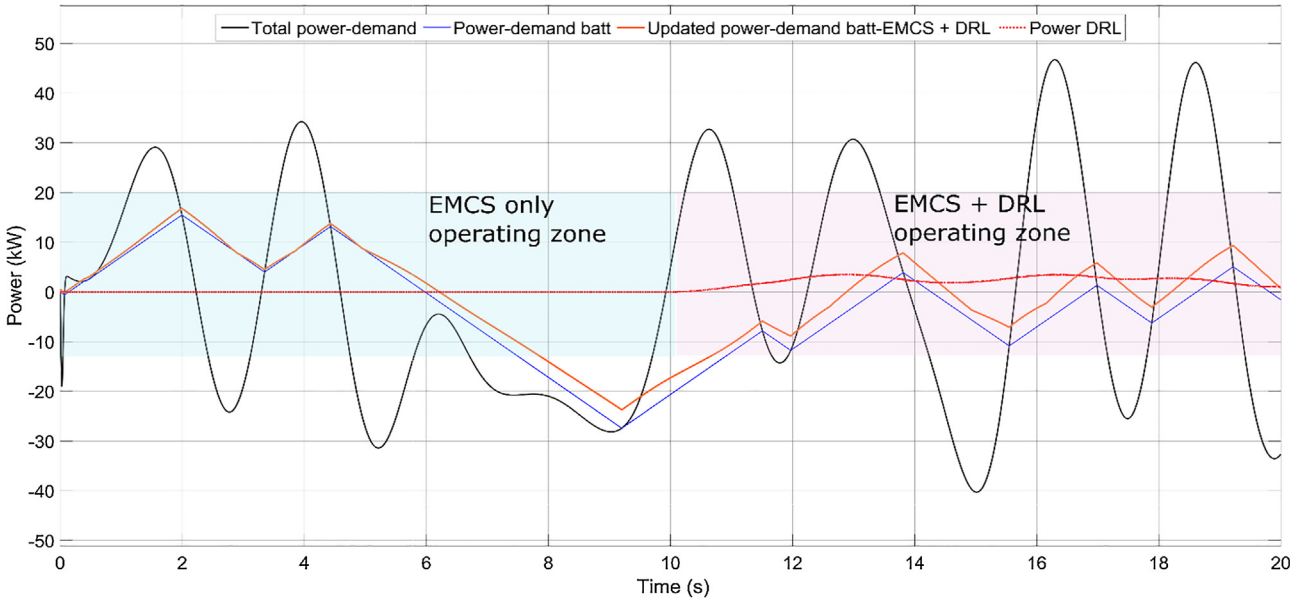

Fig. 16. Performance of the EMCS-only and the EMCS with DRL against the power demand to be stored in or supplied to the battery.

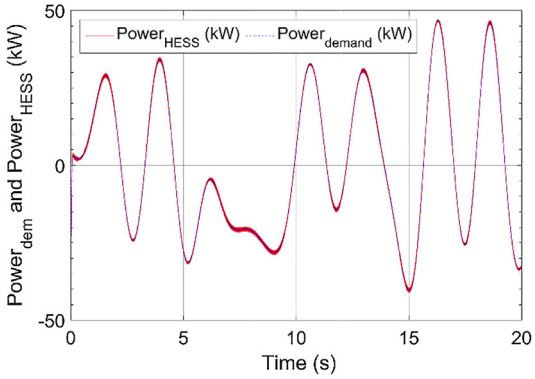

Fig. 19. Power demand for the HESS and power from the HESS.

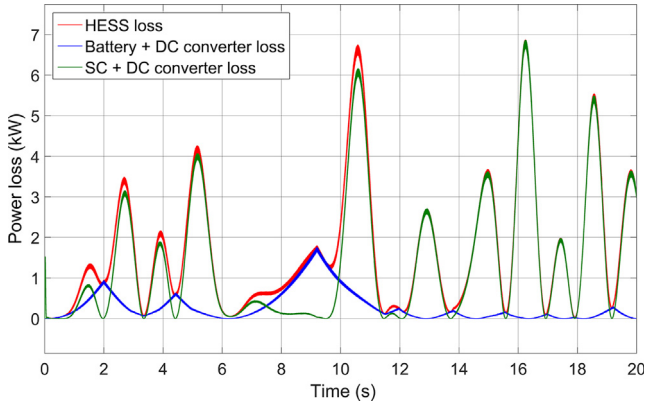

Fig. 20. Power losses of the HESS components with the EMCS-only and the EMCS with DRL operation.

difference between the oscillating total power and the average power component from the energy park. The results presented in Fig. 16 are based on the action taken by the DRL and the EMCS. Since the EMCS computes the power distribution to reduce the stress on the battery, and the DRL adjusts the SOC of the battery effectively within the SOC limits, violation conditions are handled by correcting the power demand value for the battery. Fig. 16 depicts the control of two zones, EMCS-only and EMCS with DRL in SOC limits violation conditions at 10 s. In order to demonstrate the effectiveness of the DRL, the battery SOC upper and lower limits are set to 68% and 30%, respectively.

The EMCS-only and the EMCS with DRL zone provide a stable and effective control for the battery to keep the SOC within the allowed SOC limits. Fig. 17 shows the battery response. At $t = 10$ s, the battery SOC breaks the upper limit. The DRL takes action to control the SOC by computing ΔP_{Batt} and a power demand $P^{r}_{Batt}(\Delta t)$ is updated for the controller. The performance of the EMCS-only zone can be noticed at $t = 0$ to 10 s (see Fig. 16) where the EMCS controls the power demand for the battery to reduce the stress. An initial power demand to the battery is generated by extracting the low-frequency power components from the total power demand and the extracted power is further computed in the EMCS in a loop to update a new demand, shown by the blue line. The computing power is the power demand updated for the battery shown by the orange line. The EMCS delivers this new demand to the controller of the battery and rest of the power demand goes to the controller of the SC. This is a desired behavior since the SC control is designed to handle low-frequency power components as well, which provides better stability during the power-sharing operation and removes the extra stress on the battery. At time instant $t = 10$ s, the DRL supports the EMCS until the SOC pre-set range is achieved. The DRL power is shown by the red line in Fig. 16. During operation in the allowed SOC range, the DRL power is zero due to its robust control. The SOC limits violation condition results the DRL controlling and updating the power demand to the battery. After $t = 10$ s, the DRL performs with the EMCS to bring the

SOC within the limit. Fig. 17 presents the charging and discharging of the battery module. A bidirectional DC/DC converter controls the charging and discharging current for the battery. Since the SC can absorb the extra energy and supply the current demand during another cycle of power profile from the park, the impact of the high charging and discharging current on the battery is reduced. A large voltage drop of the HESS can be avoided by operating the battery voltage in a lower fluctuation range to prevent individual cell voltage drift. Hence, the battery cell balancing situation can be avoided. A voltage variation of 7 V (300–307 V) is recorded during the simulation study. This, indeed, presents even voltage stabilization. The SOC of the battery, SOC_m, can be controlled effectively since the SC can share the high and a few low-frequency power components actively to reduce the stress and can meet the power requirement efficiently. The fast dynamic and high efficiency characteristic of the SC allows it to handle high frequency and peak current requirements.

The proposed control can guarantee the protection of the battery from fast dynamics and thus increase the battery lifetime. The SC current, the voltage and the SOC are presented in Fig. 18. A bidirectional DC/DC converter controls the SC charging and discharging. The SOC of the SC, SOC_m, is kept within the allowed range of variation and can achieve the set value (76%) by implementing this control strategy. The operating voltage of the SC is kept around 300 V, and a variation of 10 V in the SC voltage is maintained. This presents a good voltage stabilization for the SC. Therefore, the battery operating condition can be optimized through the effective and more frequent contribution of the SC. The updated power demands from the EMCS for the battery and the SC are actively distributed to keep the HESS under optimized operating condition.

The results plotted in Fig. 15 show the power distribution between the battery and the SC from Eq. (4). The power demand for the battery and SC are addressed effectively and efficiently to meet the total power demand. A positive total power demand is the extra amount of power to be stored in the HESS and a negative power demand is the surplus power from the HESS keeping the DC-grid stable at the desired value. The implemented control strategy guarantees the smoothening of the power feed to the local grid. The total power demand addressed by the HESS based on the EMCS and the DRL control is shown in Fig. 19. Figs. 15–17 depict the control of the DC/DC converter in the buck-boost mode for the battery. The WEP generates an extra amount of power during 0.2–2.2 s that gives a positive value to the HESS total power demand ($P_{HESS}(t)$) and hence both the converters act in buck-mode to store this extra power in the HESS.

Consequently, during the next period of time from $t = 2.2$ s to $t = 3.35$ s the DC/DC converter connected to SC, switched to a boost mode of operation.

This mode of operation not only supplies the surplus amount of power to maintain a stable DC-grid voltage but also charges the battery to avoid a fast drop in the battery current. It is worth noting that at 6.22 s the battery and the SC both supply a surplus amount of power to the DC-grid together until $P_{HESS}(t)$ becomes positive at 9.5 s. In Figs. 15 and 16, after 9.5 s the SC converter changes the mode to buck-operation to store the power from the WEP. During this operation, the SC is charged by the battery to maintain the SOCs in the allowed limits and reduce the losses on the battery. This mode of operation reduces the losses over the battery and the SC by sharing the power demand in a feasible amount. Therefore, a fast drop in the electrical quantities of the battery can be avoided. Fig. 20 presents the power losses of the HESS components compensated by the control. From the results, it can be appreciated that the proposed control compensates the losses evenly over the HESS components. It can be observed that the DRL operating with the EMCS effectively reduces the energy and the power loss of the battery with the DC/DC controller. The losses are shared efficiently to

reduce the overall loss of the system. A reduced loss is reported for the battery and the converter connected to it.

5. Conclusion

Wave energy is an intermittent energy source, which impacts the operation of the utility or the micro-grids due to the fluctuating output power. One means of solving this problem of unstable output is to integrate the wave energy system with a hybrid energy storage system. The hybrid power source system demands a control strategy for efficient power control. Therefore, we proposed an energy management with a dynamic rate limiter control and verified this method through simulated results by comparing other known topologies. A fully-active topology is implemented and controllers are designed for the power converters (DC/DC) to achieve this purpose. The behavior and stability of the controllers are verified in Bode plots for their current controls.

The simulation results have verified the effective control of the energy management control system along with the dynamic rate limiter control. The EMCS-only and the EMCS with DRL operating zones effectively distribute the updated power commands to the battery and the supercapacitor controllers as seen in Figs. 12 and 13. The state of charges of the hybrid energy storage components are adequately controlled and the power demand is met accordingly. The energy loss is analyzed to study the effectiveness of the power converters. The energy losses over the battery, the supercapacitor and the overall loss over the hybrid energy storage system with their converters are shown in Fig. 13. It can be observed that the overall loss for the proposed fully active topology is reduced significantly to 34 kJ compared with a conventional fully-active topology (in Fig. 12(h)). The energy loss for the battery with power converter is about 6 kJ (the blue curve). As a contrast, the supercapacitor and the power converter energy loss is about 27 kJ. This is because the supercapacitor is controlled and adjusted by the power converter to meet the demand current more frequently, resulting in larger energy loss by the power converter. Therefore, it is beneficial for the full system to have the increased efficiency of the power converter to compensate the overall loss of the hybrid energy storage system. In Fig. 20, it can be seen that the average power loss obtained in the EMCS-only zone is around 1 kW while in the EMCS with DRL zone the average loss has been reduced to a great extent for the hybrid energy storage system. In the latter zone, the battery with the converter shows an extensive improvement in its performance. The energy and power losses of the battery and supercapacitor with their controllers (Figs. 13 and 20) are smoothly shared in order to keep the losses over the battery within limits. The control avoids the fast transients in the battery and prolongs the battery life. This could reduce the overall cost of the system. Therefore, this topology could be considered as an efficient, stable, and flexible method of power distribution between a battery and the supercapacitor and for an effective voltage control. It contributes to mitigating the problem of intermittent power to the grid and provides effective control of the power flow over the hybrid energy system, increasing the life of the batteries.

The proposed control method could be used and beneficial in large-scale renewable energy systems (wave, wind and solar) for mitigating the power fluctuations and delivering a smoothened average power to the local grid. In order to implement this control algorithm, the user should carefully extract the required energy content to be addressed by the hybrid energy storage system. The energy requirement defines the rating of energy storage components and can achieve a cost saving optimization, effectively. The estimation of the Bandwidth, cross-over frequency, and individual controller PI gains must be taken under concern carefully. Furthermore, the control can support the main utility grid when load leveling and peak shaving is required. A smoothening control application for wave power and wind power generation in the case of varying loads is an interesting topic for further research, and will be addressed in a separate study with an experimental verification.

Acknowledgments

The authors would like to thank STandUp for Energy, Swedish Research Council (VR) grant No. 2015-03126, Erasmus Mundus (EMINTE) Ph.D. Scholarship, Miljöfonden, ÅForsk and Carl Tryggers Stiftelsen for their support.

Appendix A. Supplementary material

Supplementary data to this article can be found online at https://doi.org/10.1016/j.apenergy.2018.09.146.

References

[1] Chiodo E, Lauria D, Pisani C. Wind farm production estimation under multivariate wind speed distribution. Clean Electr Power (ICCEP), 2013 Int. Conf.; 2013, p. 745–50.
[2] Falnes J. A review of wave-energy extraction. Mar Struct 2007;20:185–201.
[3] Appino RR, González Ordiano JÁ, Mikut R, Faulwasser T, Hagenmeyer V. On the use of probabilistic forecasts in scheduling of renewable energy sources coupled to storages. Appl Energy 2018;210:1207–18.
[4] Adefarati T, Bansal RC. Reliability and economic assessment of a microgrid power system with the integration of renewable energy resources. Appl Energy 2017;206:911–33.
[5] Mengelkamp E, Gärttner J, Rock K, Kessler S, Orsini L, Weinhardt C. Designing microgrid energy markets: a case study: The Brooklyn Microgrid. Appl Energy 2018;210:870–80.
[6] Appendini CM, Urbano-Latorre CP, Figueroa B, Dagua-Paz CJ, Torres-Freyermuth A, Salles P. Wave energy potential assessment in the Caribbean Low Level Jet using wave hindcast information. Appl Energy 2015;137:375–84.
[7] The European Marine Energy Centre Ltd. Assessment of Wave Energy Resource; 2009.
[8] Lejerskog E, Boström C, Hai L, Waters R, Leijon M. Experimental results on power absorption from a wave energy converter at the Lysekil wave energy research site. Renew Energy 2015;77:9–14.
[9] Penalba M, Giorgi G, Ringwood JV. Mathematical modelling of wave energy converters: a review of nonlinear approaches. Renew Sustain Energy Rev 2017;78:1188–207.
[10] Thorburn K, Leijon M. Analytical and circuit simulations of linear generators in farm. Proc IEEE Power Eng Soc Trans Distrib Conf 2006:495–500.
[11] Thorburn K, Bernhoff H, Leijon M. Wave energy transmission system concepts for linear generator arrays. Ocean Eng 2004;31:1339–49.
[12] Leijon M, Skoglund A, Waters R, Rehn A, Lindahl M. On the physics of power, energy and economics of renewable electric energy sources – Part I. Renew Energy 2010;35:1729–34.
[13] Skoglund A, Leijon M, Rehn A, Lindahl M, Waters R. On the physics of power, energy and economics of renewable electric energy sources – Part II. Renew Energy 2010;35:1735–40.
[14] Leijon M, Waters R, Rahm M, Svensson O, Bostrom C, Stromstedt E, et al. Catch the wave to electricity. IEEE Power Energy Mag 2009;7:50–4.
[15] Sathishkumar R, Kollimalla SK, Mishra MK. Dynamic energy management of micro grids using battery super capacitor combined storage. 2012 Annu IEEE India Conf INDICON 2012; 2012. p. 1078–83.
[16] Abbey C, Strunz K, Joos G. A knowledge-based approach for control of two-level energy storage for wind energy systems. IEEE Trans Energy Convers 2009;24:539–47.
[17] Aneke M, Wang M. Energy storage technologies and real life applications – a state of the art review. Appl Energy 2016;179:350–77.
[18] Hasan NS, Hassan MY, Majid MS, Rahman HA. Review of storage schemes for wind energy systems. Renew Sustain Energy Rev 2013;21:237–47.
[19] Fernão Pires V, Romero-Cadaval E, Vinnikov D, Roasto I, Martins JF. Power converter interfaces for electrochemical energy storage systems – a review. Energy Convers Manage 2014;86:453–75.
[20] Chen H, Cong TN, Yang W, Tan C, Li Y, Ding Y. Progress in electrical energy storage system: a critical review. Prog Nat Sci 2009;19:291–312.
[21] Beaudin M, Zareipour H, Schellenberg A, Rosehart W. Energy storage for mitigating the variability of renewable electricity sources. Energy Storage Smart Grids Plan Oper Renew Var Energy Resour 2014:1–33.
[22] Yekini Suberu M, Wazir Mustafa M, Bashir N. Energy storage systems for renewable energy power sector integration and mitigation of intermittency. Renew Sustain Energy Rev 2014;35:499–514.
[23] Teleke S, Baran ME, Bhattacharya S, Huang AQ. Rule-based control of battery energy storage for dispatching intermittent renewable sources. IEEE Trans Sustain Energy 2010;1:117–24.
[24] Zeng J, Zhang B, Mao C, Wang Y. Use of battery energy storage system to improve the power quality and stability of wind farms. 2006 Int Conf Power Syst Technol 2006:1–6.
[25] Hredzak B, Agelidis VG, Jang M. A model predictive control system for a hybrid battery-ultracapacitor power source. IEEE Trans Power Electron 2014;29:1469–79.
[26] Zhang Q, Deng W, Zhang S, Wu J. A rule based energy management system of experimental battery/supercapacitor hybrid energy storage system for electric

vehicles. J Control Sci Eng 2016;2016:18–20.
[27] Mendis N, Muttaqi KM, Perera S. Active power management of a super capacitor-battery hybrid energy storage system for standalone operation of DFIG based wind turbines. Conf Rec – IAS Annu Meet (IEEE Ind Appl Soc) 2012.
[28] Glavin MEE, Chan PKW, Armstrong S, Hurley WGG. A stand-alone photovoltaic supercapacitor battery hybrid energy storage system. 2008 13th Int Power Electron Motion Control Conf EPE-PEMC 2008 2008:1688–95.
[29] Lahyani A, Venet P, Guermazi A, Troudi A. Battery/supercapacitors combination in uninterruptible power supply (UPS). IEEE Trans Power Electron 2013;28:1509–22.
[30] Wang Y, Liu C, Pan R, Chen Z. Modeling and state-of-charge prediction of lithium-ion battery and ultracapacitor hybrids with a co-estimator. Energy 2017;121:739–50.
[31] Ma T, Yang H, Lu L. Development of hybrid battery-supercapacitor energy storage for remote area renewable energy systems. Appl Energy 2015;153:56–62.
[32] Olabi AG. Renewable energy and energy storage systems. Energy 2017.
[33] Greenwood DM, Lim KY, Patsios C, Lyons PF, Lim YS, Taylor PC. Frequency response services designed for energy storage. Appl Energy 2017;203:115–27.
[34] Dali M, Belhadj J, Roboam X. Hybrid solar-wind system with battery storage operating in grid-connected and standalone mode: control and energy management – experimental investigation. Energy 2010;35:2587–95.
[35] Colmenar-Santos A, Linares-Mena AR, Velázquez JF, Borge-Diez D. Energy-efficient three-phase bidirectional converter for grid-connected storage applications. Energy Convers Manage 2016;127:599–611.
[36] Qian H, Zhang J, Lai JS, Yu W. A high-efficiency grid-tie battery energy storage system. IEEE Trans Power Electron 2011;26:886–96.
[37] Tedeschi E, Santos-Mugica M. Modeling and control of a wave energy farm including energy storage for power quality enhancement: the bimep case study. IEEE Trans Power Syst 2014;29:1489–97.
[38] Brando G, Dannier A, Del Pizzo A, Di Noia LP, Pisani C. Grid connection of wave energy converter in heaving mode operation by supercapacitor storage technology. Renew Power Gener IET 2016;10:88–97.
[39] Pavković D, Lobrović M, Hrgetić M, Komljenović A. A design of cascade control system and adaptive load compensator for battery/ultracapacitor hybrid energy storage-based direct current microgrid. Energy Convers Manage 2016;114:154–67.
[40] Hannan MA, Azidin FA, Mohamed A. Multi-sources model and control algorithm of an energy management system for light electric vehicles. Energy Convers Manage 2012;62:123–30.
[41] Parwal A, Remouit F, Hong Y, Francisco F, Castellucci V, Hai L, et al. Wave Energy Research at Uppsala University and The Lysekil Research Site , Sweden : A Status Update. In: Proc 11th Eur Wave Tidal Energy Conf; 2015.
[42] Thorburn K, Leijon M. Farm size comparison with analytical model of linear generator wave energy converters. Ocean Eng 2007;34:908–16.
[43] Boström C, Waters R, Lejerskog E, Svensson O, Stålberg M, Strömstedt E, et al. Study of a wave energy converter connected to a nonlinear load. IEEE J Ocean Eng 2009;34:123–7.
[44] Boström C, Lejerskog E, Stålberg M, Thorburn K, Leijon M. Experimental results of rectification and filtration from an offshore wave energy system. Renew Energy 2009;34:1381–7.
[45] Göteman M. Wave energy parks with point-absorbers of different dimensions. J Fluids Struct 2017;74:142–57.
[46] Göteman M, Engström J, Eriksson M, Isberg J. Fast modeling of large wave energy farms using interaction distance cut-off. Energies 2015;8:13741–57.
[47] Aubry J, Bydlowski P, Multon B, Ahmed H Ben, Borgarino B. Energy storage system sizing for smoothing power generation of direct wave energy converters. In: Proc 3rd Int Conf Ocean Energy (ICOE 2010), 2010, p. ISBN 978-84-693-5467-4.
[48] Thounthong P, Rael S. The benefits of hybridization. Ind Electron Mag IEEE 2009;3:25–37.
[49] Cabrane Z, Ouassaid M, Maaroufi M. Analysis and evaluation of battery-supercapacitor hybrid energy storage system for photovoltaic installation. Int J Hydrogen Energy 2016;41:20897–907.
[50] Jing W, Lai CH, Wong WSH, Wong MLD. A comprehensive study of battery-supercapacitor hybrid energy storage system for standalone PV power system in rural electrification. Appl Energy 2018;224:340–56.
[51] Choi M-E, Kim S-W, Seo S-W. Energy management optimization in a battery/supercapacitor hybrid energy storage system. IEEE Trans Smart Grid 2012;3:463–72.
[52] Dougal RA, Liu S, White RE. Power and life extension of battery-ultracapacitor hybrids. IEEE Trans Components Packag Technol 2002;25:120–31.
[53] Aktas A, Erhan K, Ozdemir S, Ozdemir E. Experimental investigation of a new smart energy management algorithm for a hybrid energy storage system in smart grid applications. Electr Power Syst Res 2017;144:185–96.
[54] Nguyen A, Lauber J, Dambrine M. Optimal control based algorithms for energy management of automotive power systems with battery/supercapacitor storage devices. Energy Convers Manage 2014;87:410–20.
[55] Song Z, Hofmann H, Li J, Hou J, Han X, Ouyang M. Energy management strategies comparison for electric vehicles with hybrid energy storage system. Appl Energy 2014;134:321–31.
[56] Khaligh A, Li Z. Battery, ultracapacitor, fuel cell, and hybrid energy storage systems for electric, hybrid electric, fuel cell, and plug-in hybrid electric vehicles: state of the art. IEEE Trans Veh Technol 2010;59:2806–14.
[57] Kuperman A, Aharon I, Malki S, Kara A. Design of a semiactive battery-ultracapacitor hybrid energy source. IEEE Trans Power Electron 2013;28:806–15.
[58] Herrera VI, Gaztañaga H, Milo A, Saez-De-Ibarra A, Etxeberria-Otadui I, Nieva T. Optimal energy management and sizing of a battery-supercapacitor-based light rail vehicle with a multiobjective approach. IEEE Trans Ind Appl 2016;52:3367–77.
[59] Song Z, Hou J, Hofmann H, Li J, Ouyang M. Sliding-mode and Lyapunov function-based control for battery/supercapacitor hybrid energy storage system used in electric vehicles. Energy 2017;122:601–12.
[60] Zhang J, Lai JS, Yu W. Bidirectional DC-DC converter modeling and unified controller with digital implementation. Conf Proc – IEEE Appl Power Electron Conf Expo – APEC 2008:1747–53.
[61] Dixon L. Average current mode control of switching power supplies. Unitrode Switch Regul Power Supply Des Appl Note 1990;3(356-3):369.
[62] Jin Y, Xu J, Zhou G, Mi C. Small signal modeling of digital V2 control for buck converter with pulse frequency modulation. Int Symp Power Electron Distrib Gener Syst IEEE 2010:102–5.
[63] Men HS, Chen D, Chang WH. Small-signal modeling of DC converters with digital peak-current-mode control. PESC Rec – IEEE Annu Power Electron Spec Conf 2008:3266–71.